

# Kolmogorov-Arnold Vision Transformer for Image Reconstruction in Lung Electrical Impedance Tomography

IBRAR AMIN, SHUAIKAI SHI , HASAN ALMARZOUQI  (Senior Member, IEEE),  
ZEYAR AUNG  (Senior Member, IEEE), WAQAR AHMED , AND PANOS LIATSIS  (Senior Member, IEEE)

Department of Computer Science, Khalifa University, Abu Dhabi 127788, UAE

CORRESPONDING AUTHOR: PANOS LIATSIS (email: panos.liatsis@ku.ac.ae).

The work was supported by ASPIRE UAE under Grant AARE20-154.

**ABSTRACT** Electrical impedance tomography is a non-invasive and non-ionizing imaging technique, which can provide real-time monitoring of the internal structures and function of the human body, and has been particularly popular in lung monitoring. However, the associated inverse problem is ill-posed, leading to suboptimal image quality with low spatial resolution, which hinders its practical use in the clinical settings. To achieve reliable image reconstruction, this work proposes a novel deep learning approach, applied to lung monitoring. The proposed model is a hybrid of the vision transformer and the recently introduced Kolmogorov Arnold Network (KAN). The fully connected layers in the transformer are replaced with KAN layers, which enhances its ability to learn the complex relationship between the voltage measurements and the conductivity distribution within the lungs. In comparison with the use of convolutional models and Vision Transformer, the proposed method achieves outstanding performance with a mean squared error of 0.0045, structural similarity index of 0.96, relative error of 0.11, and correlation coefficient of 0.98.

**INDEX TERMS** Deep learning, electrical impedance tomography, kolmogorov-Arnold networks, lung imaging, vision transformer.

## I. INTRODUCTION

Lung monitoring is considered a crucial aspect in observing the health of patients with pulmonary conditions [1]. It plays a significant role in the diagnosis of various respiratory diseases and provides valuable information on their progression and treatment effectiveness. Computed Tomography (CT) and Magnetic Resonance Imaging (MRI) are routinely used in lung imaging, however, they tend to be expensive and rely on ionizing radiation, rendering them unsuitable for continuous monitoring applications [2]. Over the past years, Electrical Impedance Tomography (EIT) has emerged as an attractive alternative, which has the potential to overcome the limitations of traditional imaging modalities. Compared with CT and MRI, EIT has the advantages of being non-ionizing, low-cost, and portable, making it suitable for continuous and bedside real-time use [3].

EIT for lung monitoring involves passing a small alternating electrical current through the electrodes, placed on

a plane, along the boundary of the thoracic region of the body, and measuring the resulting voltages on the surface. The acquired data is processed through the solution of the inverse problem to reconstruct a cross-sectional image, depicting changes in the conductivity distribution of the lungs (Fig. 1). The reconstructed image provides valuable insights into the physiological changes occurring in the lungs, such as changes in ventilation and perfusion [4], [5]. However, EIT image reconstruction is challenging due to the ill-posed and under-determined nature of the inverse problem, leading to the challenges of low spatial resolution and high sensitivity to noise [6]. Due to these limitations, the EIT inverse problem has remained an active area of research, with various approaches being proposed to enhance the quality of the reconstructed images. In the early days of EIT, one-step (direct) methods were utilized for image reconstruction. These methods linearize the problem and incorporate prior information, typically using Tikhonov (L2-norm) regularization,

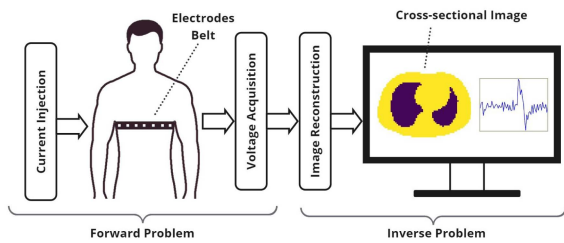


**FIGURE 1.** Flow diagram illustrating a general setup for EIT-based lung monitoring. A current source injects electric current into the thoracic region through a pair of electrodes and the resulting potentials are collected at the surface from the remaining electrodes. The inner distribution is reconstructed from the recorded potentials using a reconstruction algorithm.

to stabilize the reconstruction process [7]. Later on, iterative methods and generalized Tikhonov regularization were introduced to address the non-linear nature of the inverse problem. Iterative methods start with an initial hypothesis of the conductivity distribution and iteratively update it by minimizing the difference between the measured and simulated boundary data [7]. However, L2-based methods tend to oversmooth sharp conductivity contrasts, limiting their ability to capture fine structural details [8]. Beyond L2 regularization, L1-norm based techniques have gained attention due to their ability to enforce sparsity, thus preserving sharp edges. However, in general EIT applications, the underlying conductivity distribution may not be sparse, but instead exhibit smooth variations and multi-level contrasts. Subsequently, this may force the resulting solution to be excessively piecewise constant, suppressing subtle yet important conductivity changes. A principal example of the use of the L1-norm is Total Variation (TV) regularization, which effectively preserves sharp discontinuities in images, while removing noise and other unwanted artifacts [9]. A key drawback of TV is that it is computationally demanding due to its non-differentiability [10]. Later, algorithms like the Alternating Direction Method of Multipliers (ADMM) [10] and the Bregman-distance techniques [11], [12] were proposed to overcome the problem of non-differentiability of TV by providing more efficient solutions. While these classical approaches have shown promising results, there is a lack of a systematic methodology for the selection of their hyperparameters, which impacts the quality of the resulting solution, algorithmic stability, and convergence speed, making these methods difficult to use and time-consuming [6].

With advancements in deep learning (DL), data-driven techniques have proved to be an effective way of overcoming the limitations of traditional methods in EIT [13]. When trained on large and diverse datasets, DL models can effectively learn the complex relationship between the measured voltages and the underlying conductivity distributions, thereby improving the accuracy and spatial resolution of EIT images. Convolution-based neural networks have been an ideal choice for EIT reconstruction in various applications due to their ability to extract and learn local features [14], [15].

Such network architectures have also been widely adopted for lung EIT reconstruction, either as standalone reconstruction models or in combination with traditional techniques. Zhu et al. proposed a UNet-based architecture with reduced parameters for EIT-based monitoring of lungs during different breathing phases [16]. Zhang et al., employed a two-step framework to monitor various lung injuries using EIT [17]. They utilized a traditional optimization method to obtain the initial conductivity estimations, which were then refined using a V-shaped convolutional neural network (CNN). Similarly, in another study, the authors combined a trainable pre-constructor and a CNN-based post-processor with residual blocks to reconstruct lung shapes in various cases of injuries [18]. Yu et al. proposed a structure-aware hybrid model that achieved high-quality lung reconstructions in EIT with strong robustness [19]. The dual-branch model fuses the predicted segmentations from the visual attention net and the initial conductivity distributions from the U-Net to obtain the final reconstructions. Several studies have also reported on convolution-based generative adversarial networks (GANs) and their variants for EIT-based lung reconstruction with outstanding performance [20], [21], [22]. More recently, DL methods integrating classical regularization, particularly L1 based methods, have also been explored in EIT reconstruction [23], [24]. In the context of lung EIT, Liu et al. proposed an untrained Neural Network (NN) prior-based approach. The authors utilized a three-layer NN as a shallow image prior along with TV regularization for EIT lung reconstruction. The proposed method demonstrated major improvements and artifact removal as compared to the classical methods [25]. However, these approaches report limitations in preserving structural information and discriminative ability, while suffering from computational inefficiency.

Over the past few years, DL has witnessed a paradigm shift from the traditional convolution-based methods towards the transformer-based models. CNNs are designed with local receptive fields and impose an inductive bias towards capturing spatial hierarchies and local patterns, which limits their ability to capture relationships beyond local regions [26]. In contrast, transformers are convolution-free and come with a more general architecture, which utilizes the self-attention mechanism [27] (Fig. 3). Transformers process the entire input as a sequence of patches, and the self-attention mechanism allows them to dynamically weigh the importance of these patches relative to each other. As a result, they are able to capture long-range dependencies and global context, enabling them to surpass CNNs in a variety of computer vision tasks [26], [28], [29]. These capabilities make transformers an attractive choice for EIT lung imaging. In addition to the self-attention module, the Transformer architecture accommodates multi-layer perceptron (MLP) layers. These MLP layers have fixed activation functions, which may limit their capability to accurately represent complex functions [30]. Similarly, MLP layers have poor scaling law, meaning that the number of parameters does not scale linearly with the number of layers [31]. As an alternative to the MLP, the

Kolmogorov-Arnold Network (KAN) model [30] was recently introduced and has since captured significant attention within the AI community. Unlike MLPs, which rely on the universal approximation theorem [32], KANs are based on the Kolmogorov-Arnold representation theorem [33], [34]. KAN layers are also fully connected in nature, however, they do not have fixed activation functions on their nodes. Instead, the edges between neurons use learnable 1D activation functions parameterized as splines (Fig. 4). The neurons within a layer aggregate input without applying any non-linear activation function. In other words, KANs combine MLPs with learnable spline activations, which not only provide them with the means to learn appropriate features but also to optimize them to a high degree of accuracy [30]. This innovative design of KAN layers enhances the accuracy and interpretability of the networks, leading to comparable and often superior performance to MLPs [31], [35].

Given the promising potential of transformers and KAN, in this study, we propose a hybrid approach for EIT lung reconstruction, which incorporates KAN layers into a vision transformer (ViT), a variant of the original transformer, designed for computer vision tasks [36]. Specifically, the MLP layers in the ViT are replaced with KAN layers, thus leveraging the strengths of both architectures. This hybrid approach aims at enhancing image quality, potentially advancing the clinical applications of EIT. The main contributions of this work can be summarized as:

- 1) A ViT-based model for lung EIT reconstruction is proposed, which to the best of the authors' knowledge has not been previously investigated.
- 2) A novel hybrid model is introduced, which integrates KAN layers within the ViT architecture for high-quality image reconstruction. The use of KAN layers, which have learnable 1D activation functions, enhances the model's ability to accurately represent complex functions, compared to the standard ViT model, which uses MLPs with fixed activation functions.
- 3) The proposed method is applied on a dataset of voltage measurements and corresponding conductivity distributions, generated from real-world CT images for training and evaluation of the model.
- 4) The presented method is extensively evaluated against traditional and CNN-based EIT reconstruction methods, demonstrating superior performance on various metrics.

The rest of this article is organized as follows. The following section presents the mathematical formulation of EIT, introducing the fundamental operations of the forward and inverse problems. The Model Architecture section presents the architecture of the proposed hybrid model. The Methodology section discusses the major steps in the experiments, i.e., data collection, lung segmentation from the CT images, the solution of the EIT forward problem, and the experimental setup used for the training and evaluation of the model. The next section provides the results of the proposed architecture, including comparisons with the state-of-the-art, an analysis

of robustness to noise and computational complexity, a discussion on the impact of variation in data on the model, and the performance on the real dataset. The final section of the manuscript summarizes the achievements of the research and identifies opportunities for further work.

## II. EIT MATHEMATICAL FORMULATION

The EIT process generally consists of two interconnected sub-problems, i.e., the forward and the inverse, respectively (Fig. 1). The forward problem is the process of determining the potential difference ( $\Phi$ ) given the conductivity distribution ( $\varphi$ ) of the domain ( $\Omega$ ) and the electric current ( $I$ ) injected through the electrodes at the boundary ( $\partial\Omega$ ). Based on Maxwell's equations the forward problem is formulated as:

$$\Delta \cdot [(\varphi(x) \Delta \Phi(x, \omega))] = 0 \quad \text{in } \Omega \quad (1)$$

With the Neumann boundary condition,  $x \in \partial\Omega$

$$\varphi(x) \frac{\partial \Phi(x, \omega)}{\partial n} = I(x, \omega) \text{ at } \partial\Omega, \quad \int_{\partial\Omega} I(x, \omega) ds(x) = 0, \quad (2)$$

where  $n(x)$  is the outer normal and  $\omega$  is the angular frequency.

For domains with irregular and complex shapes, the forward problem is addressed using the finite element method (FEM). This involves dividing the conductivity domain into smaller elements and calculating the potential at each element using a linear interpolation polynomial [37]. The potential within these elements is approximated by employing basis functions, which transform the forward problem into a linear system of equations:

$$\mathbf{M} \cdot \Phi = I, \quad (3)$$

where  $\mathbf{M}$  is the conductivity matrix. The inverse problem in EIT, on the other hand, aims at reconstructing the conductivity distribution from the measured voltage data. The problem is usually solved using Taylor series expansion of the forward problem. The sensitivity matrix, i.e., the Jacobian, is determined, which serves as the mapping between variations in the conductivity distribution and the corresponding changes in the measured voltages. The computation of the sensitivity matrix involves perturbing the conductivity of individual mesh elements by a small amount ( $\partial\varphi$ ), and subsequently solving the forward problem to estimate the change in voltages ( $\partial V$ ) [38]:

$$J_{ij} \approx \frac{\delta V_i}{\delta \varphi}, \quad i = 1, P \quad j = 1, E, \quad (4)$$

where  $P$  and  $E$  represent the number of boundary measurements and mesh elements, respectively.

Following the calculation of the Jacobian matrix, conductivity changes can be estimated from the linearized problem as:

$$\delta V \approx J \delta \varphi + \epsilon, \quad (5)$$

where  $\epsilon$  indicates measurement noise.

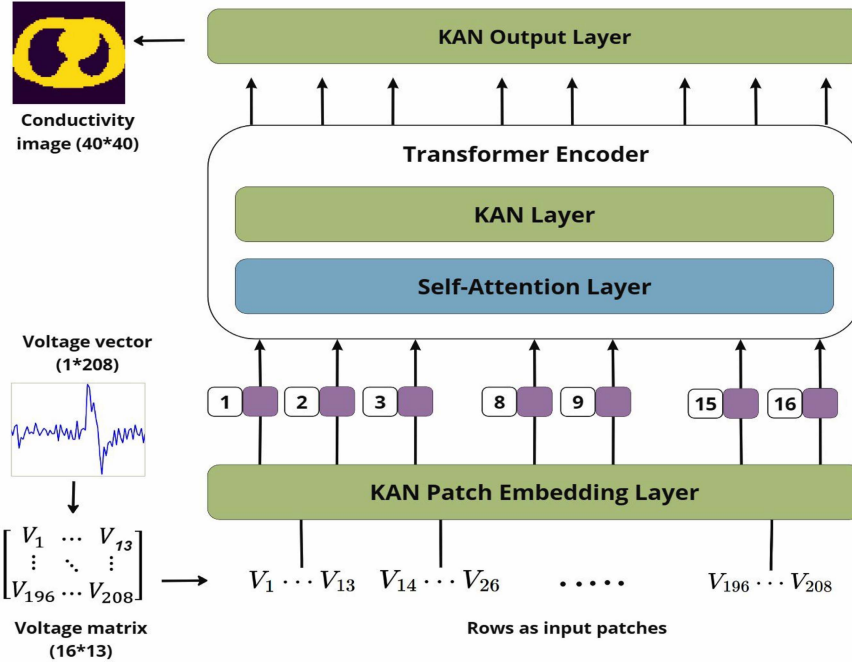


**FIGURE 2.** Flow diagram of the proposed methodology. The 1D voltage signals are processed by KAN for patch embedding, and fed to the KAN-enhanced ViT, leading to the reconstructed lung images.

Equation (5) defines a strongly ill-posed problem, which means that small changes in the voltage data may lead to arbitrarily large variations in the conductivity distribution. Indeed, the inverse problem may not have a unique stable solution [39]. A common approach to resolve the ill-conditioning of the inverse problem is to incorporate a regularization term, for instance, by using the Tikhonov prior [40], into the objective function to impose smoothness constraints on the solution, essentially stabilizing the inversion process. The regularized minimization problem can be expressed as [37]:

$$\min_{\delta\varphi} \|J\delta\varphi - \delta V\|_2^2 + \alpha^2 \|R(\delta\varphi)\|_2^2, \quad (6)$$

where  $\alpha$  is the regularization term and  $R$  is the prior.

### III. MODEL ARCHITECTURE

The proposed hybrid framework for EIT-based lung monitoring incorporates ViT as the foundational architecture and replaces the MLP layers with KAN layers to enable more efficient reconstruction of conductivity distributions from the measured voltages. As shown in Fig. 2, the overall architecture of the model consists of a transformer encoder with single-head attention. The model takes 208-dimensional voltage measurement vectors as inputs and generates conductivity images of size  $40 \times 40$  pixels. For each input, the voltage values corresponding to each current injection are considered a patch, resulting in 16 patches of size 13. The input patches undergo processing through a KAN layer to yield token embeddings of size 32 per patch. Unlike the conventional ViT, the class token is not added in the proposed architecture as it becomes redundant for the reconstruction task.

Subsequently, position embeddings are added to the token embeddings, and the resulting vectors are passed through the transformer encoder layer comprising a self-attention module and a KAN layer. Finally, the context token heads generated by the transformer encoder for the input patches are passed to the reconstruction head. The reconstruction head is a KAN layer that performs the regression task to output the final conductivity images.

#### A. SELF-ATTENTION MECHANISM

Self-Attention is the core component of the transformer architecture, which enables it to capture long-range dependencies and focus on the relevant parts of the input [27]. It involves deriving three vectors, i.e., query ( $\mathbf{q}$ ), key ( $\mathbf{k}$ ), and value ( $\mathbf{v}$ ), for all the embeddings through linear layers with learnable weights,  $\mathbf{W}_q$ ,  $\mathbf{W}_k$ , and  $\mathbf{W}_v$ , respectively. This can be expressed as:

$$\mathbf{q}^i = \mathbf{W}_q \mathbf{e}^i, \quad \mathbf{k}^i = \mathbf{W}_k \mathbf{e}^i, \quad \mathbf{v}^i = \mathbf{W}_v \mathbf{e}^i, \quad (7)$$

where ( $\mathbf{e}$ ) is an embedding with dimension  $d$  (set to 32 in this work) and position index  $i$ . The dimension  $d_m$  of all three resultant vectors is kept the same (i.e., 32), while the dimension of each weight matrix is  $d_m \times d$ . These context vectors for all the embeddings are packed together and represented as three different matrices  $\mathbf{Q}$ ,  $\mathbf{K}$ , and  $\mathbf{V}$ , each of dimension  $d_m \times n$ , where  $n$  (set to 16 in this work) is the number of tokens for each input voltage. Finally, the attention scores ( $scores$ ) are calculated using the scaled dot product between  $\mathbf{Q}$  and  $\mathbf{K}$ , followed by normalization using the softmax activation



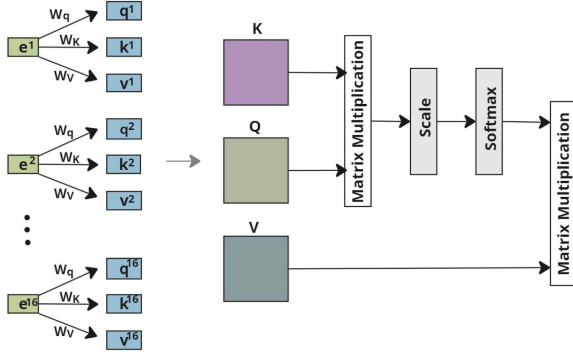


**FIGURE 3.** A visual representation of the self-attention mechanism. Each embedding is combined with weights leading to the calculation of query, key and value vectors. Context vectors for all embeddings are combined together into matrices  $\mathbf{K}$ ,  $\mathbf{Q}$ , and  $\mathbf{V}$ .

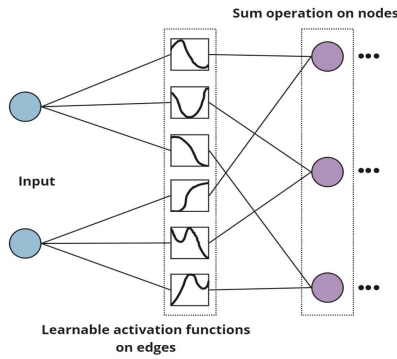


**FIGURE 4.** Architecture of KAN layer with learnable functions at edges and neurons without non-linear activation functions.

function [27]:

$$scores = softmax\left(\frac{\mathbf{QK}^T}{\sqrt{d_m}}\right) \quad (8)$$

The softmax operation produces a matrix of attention weights, which indicate the level of attention one token should give to another token. These weights are then multiplied with the  $\mathbf{V}$  vectors to produce the final output ( $Attn$ ) of the self-attention mechanism (9). The final output is the weighted sum of the values and aggregates information from all the tokens, allowing the model to capture dependencies and relationships between tokens. Fig. 3 depicts a visual illustration of the self-attention mechanism.

$$Attn = scores \cdot \mathbf{V} \quad (9)$$

## B. KAN LAYER

The KAN layers in the proposed model are adapted from the KAN model, inspired by the Kolmogorov-Arnold representation theorem [33], [34]. Like MLPs, KAN layers are fully connected in nature but do not have fixed activation functions on their nodes. Instead, the edges between neurons use learnable 1D activation functions parameterized as splines (Fig. 4). The neurons within a layer aggregate input without

applying any non-linear activation function. The combination of an architecture similar to MLP and learnable spline activations allows KAN layers to both learn and optimize features accurately [30]. Mathematically, a KAN layer ( $\mathbf{L}$ ) can be represented as a matrix of activation functions ( $\phi$ ) [30]:

$$\mathbf{L} = [\phi_{o,i}], \quad i = 1, 2, \dots, n_{in}, \quad o = 1, 2, \dots, n_{out}, \quad (10)$$

where  $n_{in}$  and  $n_{out}$  are the number of neurons in the input layer ( $I$ ) and the KAN layer, respectively. It is evident from (10) that there exist  $n_{in}n_{out}$  activation functions between the two layers. The pre-activation for a certain  $\phi_{o,i}$  is simply the signal coming from the neuron  $I_i$  in the input layer, which is processed to generate post-activation, i.e.,  $\phi_{o,i}(I_i)$ . The final value at a neuron in the KAN is the sum of all the incoming post-activations [30]:

$$L_o = \sum_{i=1}^{n_{in}} \phi_{o,i}(I_i) \quad (11)$$

Moreover, in order to improve the optimization process, a base function  $b(I)$  is incorporated, which operates similarly to the residual connections in DL models. The activation function  $\phi(I)$  can now be expressed as the sum of  $b(I)$  and the spline function:

$$\phi(I) = w_b b(I) + w_s spline(I), \quad (12)$$

where  $w_b$  and  $w_s$  are learnable parameters that control the overall magnitude of the activation function.  $b(I)$  is set to Sigmoid Linear Unit (SiLU) activation function [44]:

$$b(I) = silu(I) = \frac{I}{(1 + e^{-I})}, \quad (13)$$

and  $spline(I)$  is a linear combination of B-splines:

$$spline(I) = \sum_i z_i B_i(I), \quad (14)$$

where the  $z_i$  are trainable parameters.

## IV. METHODOLOGY

The major steps in the proposed framework are shown in Fig. 5. The dataset consists of real-world CT images which are segmented into regions of interest. Next, the segmented lung regions are discretized using FEM, and the EIT forward problem is solved, resulting in the voltage data. Lastly, the proposed model is trained and evaluated on the generated data to reconstruct the conductivity distribution of the lungs.

### A. DATA COLLECTION

The 4-D Lung CT data used for this study is obtained from The Cancer Imaging Archive (TCIA) [45]. The CT images were originally acquired during chemoradiotherapy treatment for 20 patients (labeled from 100 to 119) diagnosed with locally advanced, non-small cell lung cancer. Each patient underwent multiple scans at various time points, comprehensively capturing ten different phases (0–90%) of breathing at each interval. Each CT consists of multiple slices with an axial resolution of  $512 \times 512$  pixels. Additional information

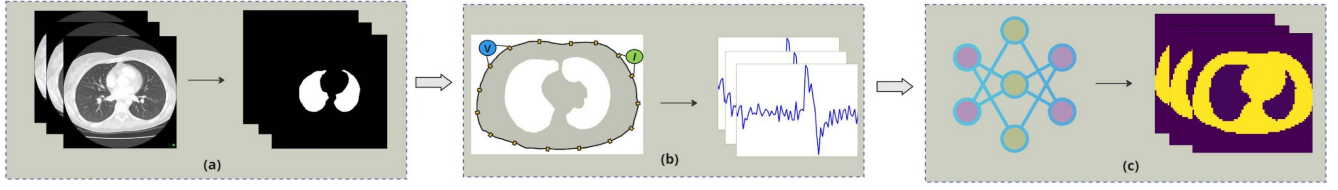


**FIGURE 5.** Workflow of the proposed methodology: (a) Segmentation of CT lung slices. (b) Forward problem simulations of the segmented lung structures in EIDORS. (c) Training the DL model for lung reconstruction.

on the dataset can be found in [46]. For this study, scans with missing lung regions, likely due to surgical removal, are excluded. These scans have irregular shapes and edges and require a different mesh refinement level, compared to normal lung scans. In order to maintain uniformity, only CT studies with complete lung shapes are considered. For the purposes of image reconstruction, the dataset is divided into 3,109 scans for training, 410 scans (from patients 102 and 107) for validation, and 400 scans (from patients 113 and 114) for testing.

### B. DATA SEGMENTATION

When using EIT for lung monitoring, the fifth intercostal space is considered the optimal position for electrode belt placement [1]. Placing the electrodes too high may affect lung compliance, while positioning them too low can result in hyperinflation [41]. To adhere to this standard, we selected the slice at the fifth intercostal space from each CT volume. Subsequently, the lungs in the selected slices are segmented using 3-D slicer [42], a widely used open-source software for medical image analysis. Finally, the segmented lung structures are integrated within the thorax shape (corresponding to the same intercostal space) to simulate the forward problem in EIT and collect the voltage data.

### C. EIT SIMULATION

The simulations are performed in MATLAB with the help of the Electrical Impedance Tomography and Diffuse Optical Tomography Reconstruction Software (EIDORS) toolbox [43]. The thorax is discretized into 6400 triangular finite elements (Fig. 6) using NETGEN within the EIDORS framework. The simulations incorporate the Complete Electrode Model (CEM), which takes into account the presence of the electrodes and the contact impedances, providing a more realistic representation of EIT measurements [50]. To facilitate the current injection and voltage measurement on the surface, sixteen electrodes are evenly spaced along the boundary. The conductivity of the background (thorax) is set to 1 S/m, while the conductivity of the inhomogeneities (lungs) is set to 0.3 S/m, following the recommended values and practice in the official EIDORS framework [51]. Using the adjacent protocol, a current of 1 mA amplitude is sequentially injected through each pair of electrodes, and the corresponding voltages are measured from the remaining of the electrode pairs, resulting in a total of 208 voltage measurements, after a complete scan. Furthermore, differential EIT is performed by acquiring the reference data using a homogenous medium (thoracic area

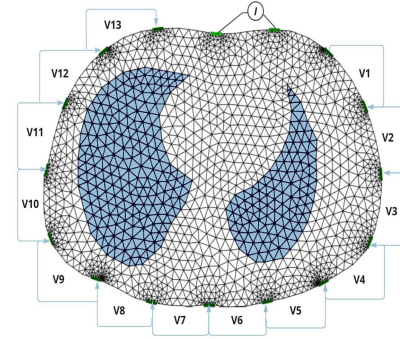


**FIGURE 6.** Illustration of the simulated thoracic region discretized into finite elements. A coarser mesh (2,591 elements) is shown for better visualization, compared to the finer mesh (6,400 elements) used in actual experiments. The EIT system comprises of sixteen electrodes for current injection and voltage measurement using the adjacent protocol.

without any lung structures) beforehand [13]. The acquired measurements are then utilized to train the DL model for reconstructing the conductivity distributions of the lungs.

### D. EXPERIMENTAL SETUP

#### 1) NETWORK TRAINING

For training, the ADAM optimization algorithm is utilized with an initial learning rate (lr) of 0.00001, which is reduced by a factor of 0.1, when the validation loss does not improve for 20 consecutive epochs. The regularized MSE ( $L_{REG}$ ) is employed as the loss function, which includes a weight decay term to prevent overfitting [47]:

$$L_{REG} = \frac{1}{N} \sum_{i=1}^N (G(\mathbf{x}_i) - \mathbf{Y}_i)^2 + \frac{\lambda}{2} \sum_j \theta_j^2, \quad (15)$$

where  $N$  is the number of samples in the training data,  $G(\cdot)$  is the non-linear function representing the proposed model,  $\mathbf{x}_i$  and  $\mathbf{Y}_i$  denote the input voltage vector and the ground truth conductivity image, respectively,  $\lambda$  is the weight decay factor (set to 0.00001), and  $\theta_j$  are model parameters.

The batch size is set to 128, and the model is trained for a total of 2500 epochs in a PyTorch-GPU environment. All the experiments are executed on a Nvidia RTX 4090 GPU.

#### 2) EVALUATION CRITERIA

To quantitatively evaluate the performance of the proposed EIT reconstruction method and the reference methods, four different metrics are calculated. These metrics are the mean

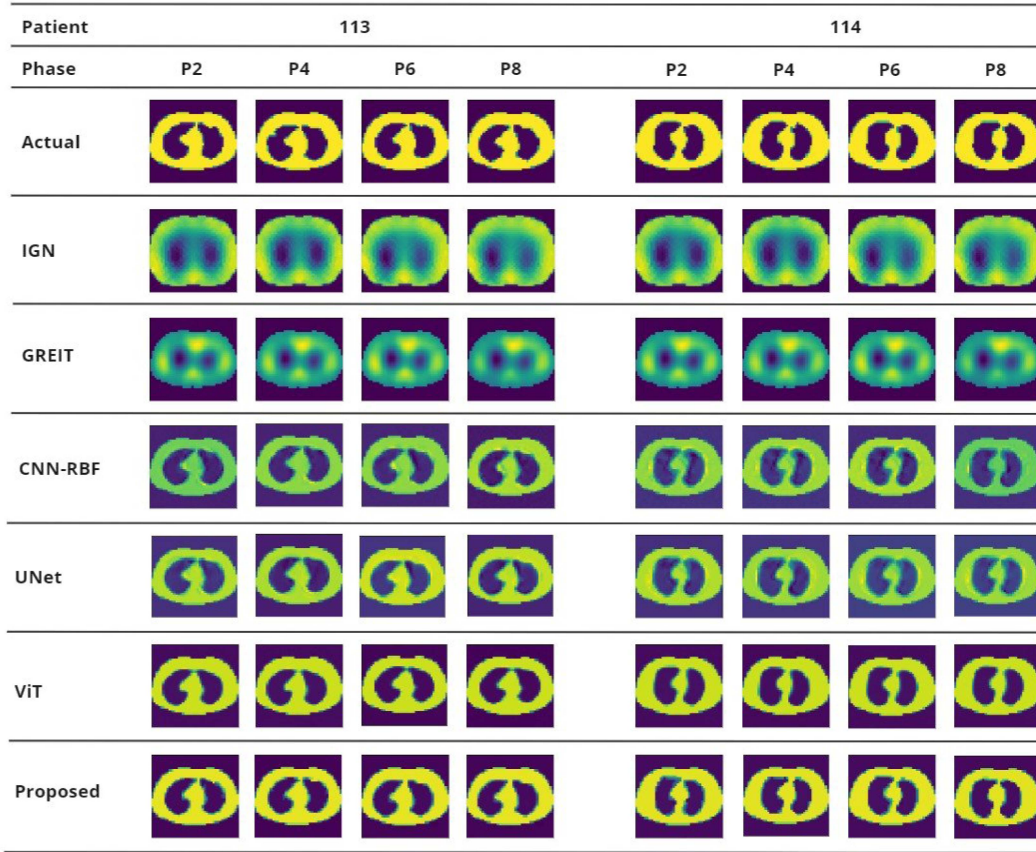


**FIGURE 7.** Representative examples of EIT-based lung reconstruction on the test set (patients 113 and 114, at different phases of breathing) with fixed thorax shape and lung conductivity. The top row provides the ground truth. The proposed KAN-enhanced ViT model is compared to two traditional optimization methods, two state-of-the-art DL models, and the standard ViT architecture.

squared error (MSE), structural similarity index (SSIM), correlation coefficient (CC), and relative image error (RIE). SSIM is a perceptual image quality metric representing non-linear changes and structural similarity between the actual ( $X$ ) and reconstructed images ( $Y$ ). It is defined as:

$$SSIM(X, Y) = \frac{(2\mu_X\mu_Y + c_1)(2\sigma_{XY} + c_2)}{(\mu_X^2 + \mu_Y^2 + c_1)(\sigma_X^2 + \sigma_Y^2 + c_2)}, \quad (16)$$

where  $\mu_X$ ,  $\mu_Y$ ,  $\sigma_X$ ,  $\sigma_Y$ , and  $\sigma_{XY}$  represent, respectively, the means, the standard deviations, and the covariance of images  $X$  and  $Y$ , while  $c_1$  and  $c_2$  are constants.

CC quantifies the strength and direction of a linear relationship between the two images. It is calculated as:

$$CC = \frac{\sigma_{XY}}{\sigma_X\sigma_Y} \quad (17)$$

RIE computes the error between the ground truth and the reconstructed image by comparing their pixel values and is defined as:

$$RIE = \frac{\|Y - X\|_2}{\|X\|_2} \quad (18)$$

## V. RESULTS AND DISCUSSION

### A. COMPARISON ON SIMULATED DATA

In this section, we present the quantitative and qualitative analysis of the proposed model performance and compare it against five baseline methods: two traditional optimization methods, two CNN-based methods, and a standard ViT. The traditional methods are the iterative Gauss-Newton (IGN) and the GREIT algorithm, both of which are well-established in the EIT field, with GREIT being specifically designed for lung EIT [48]. For the convolution-based methods, CNN-RBF and a lightweight UNet architectures are considered. Both of these DL models have shown promising performance in previous studies in EIT-based lung reconstruction [16], [49]. The ViT model follows a compact architecture that resembles the proposed model, except that it uses MLP layers and a higher embedding dimension of 128.

Fig. 7 illustrates the reconstructions in four distinct breathing phases (i.e., P2, P4, P6, P8) of patients 113 and 114 carried out by various algorithms. The EIT images reconstructed by IGN and GREIT contain noticeable blurring and noise artifacts and fail to capture the fine details in the lung regions. The poor performance of these traditional methods is also reflected in the quantitative metrics presented in Table 1, characterized by significantly higher error values and lower SSIM and CC



**TABLE 1. Quantitative Performance of Various EIT Reconstruction Algorithms on Test Data**

Method	MSE	SSIM	RIE	CC
GN	0.1521	0.2556	0.6525	0.5714
GREIT	0.1017	0.4146	0.5096	0.7502
CNN-RBF	0.0083	0.9333	0.1684	0.9554
UNet	0.0075	0.9482	0.1525	0.9623
ViT	0.0061	0.9531	0.1327	0.9750
Proposed	0.0045	0.9676	0.1109	0.9891

**TABLE 2. Computational Complexity Analysis of the Proposed and Baseline Methods**

Method	FLOPS ( $\times 10^6$ )	Training Time (h)	Inference Time (ms)
GN	-	-	31
GREIT	-	-	16
CNN-RBF	47.12	0.66	4.12
UNet	53.31	0.75	3.25
ViT	4.98	0.42	0.52
Proposed	3.53	0.50	0.65

scores. A huge improvement in the reconstruction quality is observed for the CNN-based methods. Both CNN-RBF and UNet significantly reduced the error values, and achieved much higher SSIM (0.9333 and 0.9482, respectively) and CC (0.9554 and 0.9623, respectively), when compared to IGN and GREIT. The ViT model, which relies on self-attention, instead of convolution, improved the performance further, producing reconstructions with sharper lung boundaries and enhanced contrast. It surpassed the best performing CNN (UNet) model by achieving higher SSIM and CC and lowering the values of the MSE and RIE metrics by 18.67% and 12.98%, respectively. However, some smoothing artifacts still remain visible. Interestingly, the proposed ViT with KAN layers yielded the best qualitative and quantitative results, outperforming the previous methods across all metrics. By minimizing the reconstruction errors of the ViT further, i.e., MSE by 26.23%, and RIE by 16.4%, the proposed model delivered the highest fidelity reconstructions with minimal artifacts that closely resemble the ground truth (Fig. 7). The improvements of ViT over CNN-based methods and of the proposed method over ViT demonstrate the efficacy of the self-attention mechanism, further enhanced by the KAN layers with learnable activation functions.

### B. COMPUTATIONAL COMPLEXITY ANALYSIS

The computational complexity of the evaluated reconstruction methods is summarized in Table 2. The table presents the number of floating-point operations (FLOPs) for a single forward pass, the training time for the DL-based methods, and the average reconstruction time per sample. The reconstruction time for the classical methods is calculated on an Intel Core i9-13900KF (13th Gen, 3.00 GHz) CPU, while the DL methods are evaluated on a single NVIDIA RTX 4090.

**TABLE 3. Sensitivity of the Proposed Model to Training Data Size**

Train Data	Embed Dim	Parameters ( $\times 10^6$ )	MSE	SSIM
20%	8	0.6	0.0091	0.9034
40%	16	1.2	0.0072	0.9324
60%	16	1.2	0.0057	0.9582
80%	32	2.24	0.0051	0.9628
100%	32	2.24	0.0045	0.9676

Overall, classical methods exhibit significantly higher reconstruction times compared to DL-based approaches. Among the DL models, CNN-RBF and UNet have the highest computational costs, with  $47.12 \times 10^6$  and  $53.31 \times 10^6$  FLOPs, respectively. In contrast, ViT has a much lower FLOP count at  $4.98 \times 10^6$ , resulting in the shortest inference time of 0.52 ms. The proposed model, with a slightly higher reconstruction time (0.65 ms) than ViT, is the least computationally demanding ( $3.53 \times 10^6$  FLOPs). Additionally, it achieves a favorable trade-off between inference time and reconstruction quality, as reflected in Table 1.

### C. SENSITIVITY OF THE PROPOSED MODEL TO TRAINING DATA

To assess the impact of the training data size on the performance of the proposed model, we conducted experiments using different subsets of the data, while adjusting the complexity of the model accordingly. Since the proposed model is already highly simplified, the primary factor influencing model complexity is the embedding dimension. Reducing the embedding dimension effectively reduces the number of parameters, preventing overfitting for training datasets of smaller sizes. As shown in Table 3, the performance of the model steadily improves as the training data increases from 20% to 100%, with the MSE decreasing from 0.0091 to 0.0045 and SSIM increasing from 0.9034 to 0.9676. The number of model parameters scales accordingly, from  $0.6 \times 10^6$  with an embedding dimension of 8 to  $2.4 \times 10^6$  million with an embedding dimension of 32, ensuring that the model capacity grows in proportion to the data. With careful tuning, the model is able to achieve reasonable performance even with limited training data. The largest performance gain occurs when increasing the size of the training data from 20% to 60%, after which improvements become more gradual. This suggests that while further increasing the dataset size could yield additional improvements, the diminishing returns indicate that the model has already reached near-optimal performance for this task.

### D. ROBUSTNESS OF PROPOSED MODEL TO NOISE

To demonstrate the robustness to noise properties of the proposed model, Gaussian noise of varying levels (up to 10%) was added to the input voltage signals. Table 4 presents the performance metrics for image reconstruction under various



**TABLE 4. Performance of the KAN-Enhanced ViT Architecture At Various Levels of Noise**

Noise Level	MSE	SSIM	RIE	CC
0%	0.0045	0.9676	0.1109	0.9891
3%	0.0052	0.9632	0.1170	0.9837
5%	0.0055	0.9607	0.1228	0.9799
10%	0.0062	0.9570	0.1267	0.9765

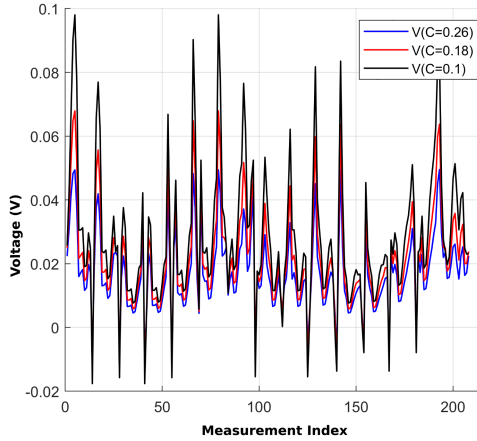


**FIGURE 8. Comparison of the voltages (V) for the same thorax shape and lung anatomy but with different lung conductivities (C). It is observed that variations in the lung conductivity between end-inhalation (0% phase) and end-exhalation (50% phase) result in measurable differences in the recorded voltages.**

levels of noise. The results illustrate the outstanding robustness of the model to noise, with RIE increasing from 0.1109 at 0% noise to only 0.1267 at 10% noise, while SSIM and CC decreasing by just 1.10% and 1.27%, respectively. Moreover, the performance achieved at 10% noise surpasses that obtained by UNet and nearly matches the results of ViT on the noise-free data. The robustness of the model to noise is crucial for real-world clinical applications, where the presence of noise in the voltage measurements is inevitable.

#### E. PERFORMANCE ON DATA WITH THORACIC AND CONDUCTIVITY VARIATIONS

While these results highlight the effectiveness of the proposed model in handling measurement noise, complexities in real-world scenarios extend beyond the presence of noise. Anatomical and physiological differences among patients introduce additional data challenges, potentially impacting on model performance. Specifically, changes in thorax shape influence the placement of surface electrodes, while variations in lung physiology during breathing alter conductivity values, thereby affecting the measured voltage patterns (Fig. 8). In order to assess the performance of the proposed model in the context of these complexities, a new set of experiments was conducted, which included individual thorax shape models for each patient, and variations in lung conductivity values between end-inhalation (0.10 S/m) and end-exhalation (0.26 S/m) [16]. In this experimental setup, the voltages are

collected using a time-difference approach, with the initial breathing state being the baseline. The model achieved excellent quantitative results on the test data with an MSE score of 0.0058, SSIM of 0.96, RIE of 0.1256, and CC of 97.60. Example reconstruction results are presented in Fig. 9, where the varying color in the lung regions represents the dynamic changes in conductivity values during the breathing process. Notably, the model was not only able to accurately reconstruct the anatomical details of the thorax and lungs but moreover, it adeptly modeled conductivity variations during the breathing cycle. These findings further underscore the potential of the proposed model in real-world clinical applications.

#### F. PERFORMANCE ON REAL DATA

To validate the capability of the proposed model on real data, we used a publicly available dataset from the EIDORS repository. The data is unlabelled and consists of 34 voltage frames, each corresponding to a different phase in a breathing cycle. Unlike the simulated voltages used in model training, the real voltage values are significantly larger in magnitude, making direct use of the trained model infeasible. To facilitate domain adaption, we performed a two-step pre-processing to bring the values of the real dataset voltages closer to those of the simulated distribution. First, the real voltages ( $V_{real}$ ) are standardized by::

$$V'_{real} = \frac{V_{real} - \mu_{real}}{\sigma_{real}}, \quad (19)$$

where  $\mu_{real}$  and  $\sigma_{real}$  are the mean and variance of the real voltages, respectively, and  $V'_{real}$  represents the standardized real voltages. Next,  $V'_{real}$  is re-scaled to match the distribution of the simulated dataset used in training:

$$V''_{real} = V'_{real} * \sigma_{sim} + \mu_{sim}, \quad (20)$$

where  $\sigma_{sim}$  and  $\mu_{sim}$  are the mean and standard deviation of simulated data, respectively, and  $V''_{real}$  denotes the re-scaled real voltages. Fig. 10 presents visual results of the reconstructed lungs at different phases of the breathing cycle. Since the dataset is unlabelled and does not provide ground truth conductivity distributions, we include the reconstructions obtained using GREIT for comparison. The thorax shape in the GREIT reconstructions is based on the predefined forward model (mk\_library\_model) in EIDORS. This does not necessarily represent the actual thorax shape in the real data but rather it reflects the assumed model geometry. As a result, the comparison between the reconstructions of the two methods is only focused on the internal conductivity distributions. It is evident from the figure that the proposed model successfully reconstructed the lung shapes across different breathing phases. Moreover, it effectively captures the expected conductivity variations, which closely align with those obtained via GREIT. These results demonstrate the potential of the proposed model for real-world applications, particularly in clinical scenarios, where real-time lung function assessment is required.

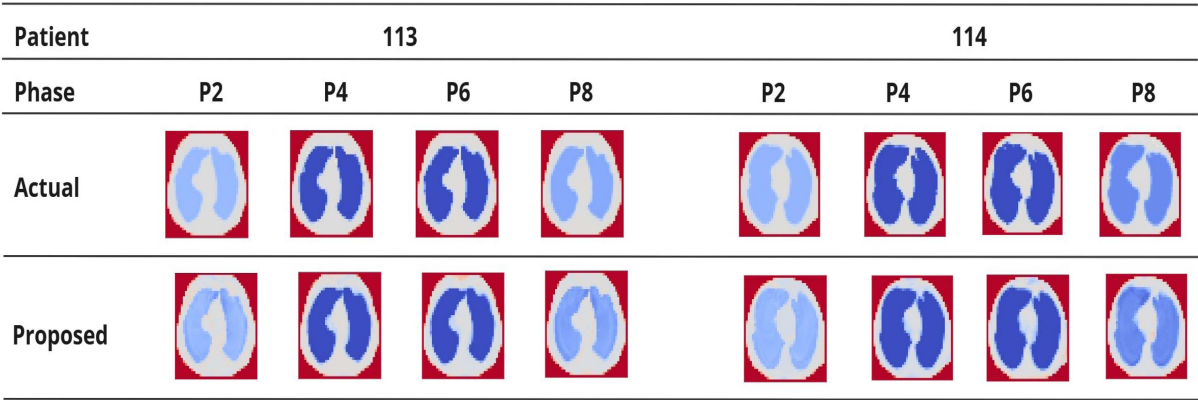


**FIGURE 9.** Representative examples of EIT-based lung reconstruction by the proposed model on the test set with varying thorax shape and lung conductivity values. The color variations in the lungs correspond to different conductivity levels across various breathing phases.

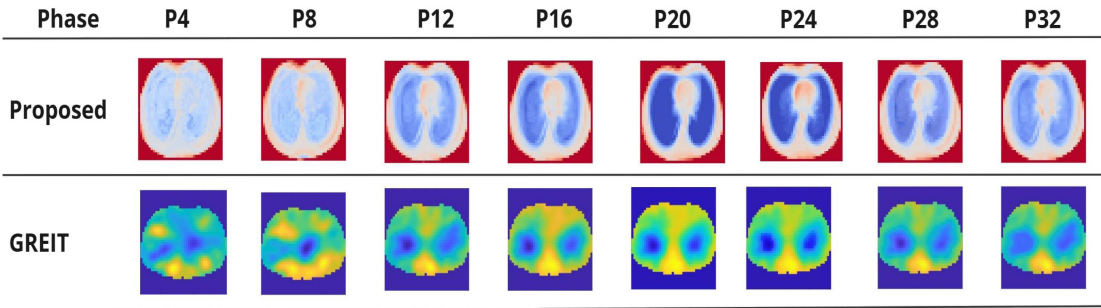


**FIGURE 10.** Representative examples of EIT-based lung reconstructions by the proposed model and GREIT on the real data. The reconstructed conductivity variations across different breathing phases show close agreement between both methods.

VI. CONCLUSION

In this article, a novel approach for lung EIT was proposed, which leverages the strengths of ViT and KAN to obtain highly reliable image reconstructions. The hybrid model leverages ViT as the backbone and incorporates KAN layers to replace the MLP layers. To assess the effectiveness of the model, it is trained and evaluated on a dataset of EIT measurement and ground-truth conductivity distributions generated from real-world lung CT scans. The proposed model performance was benchmarked against traditional optimization methods, CNNs, and the standard ViT. Results demonstrated superior reconstruction for the proposed model in terms of quantitative metrics, as well as through visual assessment. The model exhibited strong robustness to noise, outperforming the reference methods even at relatively high levels of noise. Similarly, it demonstrated high-quality reconstructions despite significant anatomical and physiological variations in the data. Experiments on the real-world data further validated the robustness and practicality of the model, highlighting its potential for clinical applications. In the future, we aim at improving the generalization of the model by extending this work to a more diverse dataset covering a wider range of lung pathologies, including various lung injury conditions.

REFERENCES

[1] V. Tomicic et al., “Lung monitoring with electrical impedance tomography: Technical considerations and clinical applications,” *J. Thoracic Dis.*, vol. 11, no. 7, pp. 3122–3135, 2019, doi: [10.21037/jtd.2019.06.27](#).

[2] R. E. Watson et al., “Safety considerations in MRI and CT,” *CON-TINUUM: Lifelong Learn. Neurol.*, vol. 29, no. 1, pp. 27–53, 2023, doi: [10.1212/CON.00000000000001213](#).

[3] L. Yang et al., “Electrical impedance tomography as a bedside assessment tool for COPD treatment during hospitalization,” *Front. Physiol.*, vol. 15, 2024, Art. no. 1352391, doi: [10.3389/fphys.2024.1352391](#).

[4] Q. Wang et al., “Early bedside detection of pulmonary perfusion defect by electrical impedance tomography after pulmonary endarterectomy,” *Pulmonary Circulation*, vol. 14, no. 2, 2024, Art. no. e12372, doi: [10.1002/pul2.12372](#).

[5] I. Fratti et al., “Electrical impedance tomography: A monitoring tool for ventilation induced lung injury,” *Amer. J. Respir. Crit. Care Med.*, vol. 209, no. 12, pp. 1510–1513, 2024, doi: [10.1164/rccm.202311-2121LE](#).

[6] C. Dimas, V. Alimisis, N. Uzunoglu, and P. Sotiriadis, “Advances in electrical impedance tomography inverse problem solution methods: From traditional regularization to deep learning,” *IEEE Access*, vol. 12, pp. 47797–47829, 2024, doi: [10.1109/ACCESS.2024.3382939](#).

[7] M. Aller, D. Mera, J. M. Cotos, and S. Villaroya, “Study and comparison of different machine learning-based approaches to solve the inverse problem in electrical impedance tomographies,” *Neural Comput. Appl.*, vol. 35, no. 7, pp. 5465–5477, 2023, doi: [10.1007/s00521-022-07988-7](#).

[8] X. Song, Y. Xu, and F. Dong, “A hybrid regularization method combining Tikhonov with total variation for electrical resistance tomography,” *Flow Meas. Instrum.*, vol. 46, pp. 268–275, Dec. 2015, doi: [10.1016/j.flowmeasinst.2015.07.001](#).

- [9] A. Borsic, B. M. Graham, A. Adler, and W. R. Lionheart, "In vivo impedance imaging with total variation regularization," *IEEE Trans. Med. Imag.*, vol. 29, no. 1, pp. 44–54, Jan. 2010, doi: [10.1109/TMI.2009.2022540](#).
- [10] A. Javaherian, M. Soleimani, K. Moeller, A. Movafeghi, and R. Faghihi, "An accelerated version of alternating direction method of multipliers for TV minimization in EIT," *Appl. Math. Modelling*, vol. 40, pp. 21–22, Nov. 2016, doi: [10.1016/j.apm.2016.05.052](#).
- [11] J. Wang, J. Ma, B. Han, and Q. Li, "Split bregman iterative algorithm for sparse reconstruction of electrical impedance tomography," *Signal Process.*, vol. 92, no. 12, pp. 2952–2961, Dec. 2010, doi: [10.1016/j.sigpro.2012.05.027](#).
- [12] F. Li, J. F. P. J. Abascal, M. Desco, and M. Soleimani, "Total variation regularization with split Bregman-based method in magnetic induction tomography using experimental data," *IEEE Sensors*, vol. 17, no. 4, pp. 976–985, Feb. 2017, doi: [10.1109/JSEN.2016.2637411](#).
- [13] F. Pennati et al., "Electrical impedance tomography: From the traditional design to the novel frontier of wearables," *IEEE Trans. Pattern Anal. Mach. Intell.*, vol. 23, no. 3, Jan. 2023, doi: [10.3390/s23031182](#).
- [14] D. Liu, J. Wang, Q. Shan, D. Smyl, J. Deng, and J. Du, "DeepEIT: Deep image prior enabled electrical impedance tomography," *IEEE Trans. Pattern Anal. Mach. Intell.*, vol. 45, no. 8, pp. 9627–9638, Aug. 2023, doi: [10.1109/TPAMI.2023.3240565](#).
- [15] Z. Wang, X. Zhang, R. Fu, D. Wang, X. Chen, and H. Wang, "Electrical impedance tomography image reconstruction with attention-based deep convolutional neural network," *IEEE Trans. Instrum. Meas.*, vol. 72, 2023, Art. no. 5011318, doi: [10.1109/TIM.2023.3265108](#).
- [16] L. Zhu, W. Lu, M. Soleimani, Z. Li, and M. Zhang, "Electrical impedance tomography guided by digital twins and deep learning for lung monitoring," *IEEE Trans. Instrum. Meas.*, vol. 72, 2023, Art. no. 4009309, doi: [10.1109/TIM.2023.3298389](#).
- [17] X. Zhang et al., "V-shaped dense denoising convolutional neural network for electrical impedance tomography," *IEEE Trans. Instrum. Meas.*, vol. 71, 2022, Art. no. 4503014, doi: [10.1109/TIM.2022.3166177](#).
- [18] S. Ren, K. Sun, C. Tan, and F. Dong, "A two-stage deep learning method for robust shape reconstruction with electrical impedance tomography," *IEEE Trans. Instrum. Meas.*, vol. 69, no. 7, pp. 4887–4897, Jul. 2020, doi: [10.1109/TIM.2019.2954722](#).
- [19] H. Yu, H. Liu, Z. Liu, Z. Wang, and J. Jia, "High-resolution conductivity reconstruction by electrical impedance tomography using structure-aware hybrid-fusion learning," *Comput. Methods Programs Biomed.*, vol. 243, 2024, Art. no. 107861, doi: [10.1016/j.cmpb.2023.107861](#).
- [20] X. Li, R. Zhang, Q. Wang, X. Duan, Y. Sun, and J. Wang, "SAR-CGAN: Improved generative adversarial network for EIT reconstruction of lung diseases," *Biomed. Signal Process. Control*, vol. 81, Mar. 2023, Art. no. 104421, doi: [10.1016/j.bspc.2022.104421](#).
- [21] M. Zhao et al., "Application of electrical impedance tomography imaging technology combined with generative adversarial network in pulmonary ventilation monitoring," *J. Biomed. Eng.*, vol. 41, no. 1, pp. 105–113, Feb. 2024, doi: [10.7507/1001-5515.202308026](#).
- [22] X. Li, R. Zhang, Q. Wang, X. Duan, and J. Wang, "Lung electrical impedance tomography based on improved generative adversarial network," in *Web and Big Data. APWeb-WAIM 2022 International Workshops*, S. Yang and S. Islam eds. Berlin, Germany: Springer, 2022, pp. 138–150, doi: [10.1007/978-981-99-1354-1-13](#).
- [23] Z. Chen, J. Xiang, P.-O. Bagnaninchi, and Y. Yang, "MMV-net: A multiple measurement vector network for multifrequency electrical impedance tomography," *IEEE Trans. Neural Netw.*, vol. 34, no. 11, pp. 8938–8949, Nov. 2023, doi: [10.1109/TNNLS.2022.3154108](#).
- [24] Z. Chen, Y. Yang, and P.-O. Bagnaninchi, "Hybrid learning-based cell aggregate imaging with miniature electrical impedance tomography," *IEEE Trans. Instrum. Meas.*, vol. 70, 2020, Art. no. 4001810, doi: [10.1109/TIM.2020.3035384](#).
- [25] Z. Liu, Z. Chen, H. Fang, Q. Wang, S. Zhang, and Y. Yang, "Regularized shallow image prior for electrical impedance tomography," *IEEE Trans. Instrum. Meas.*, vol. 74, no. 11, 2025, doi: [10.1109/TIM.2025.3545548](#).
- [26] J. Mauricio, I. Domingues, and J. Bernardino, "Comparing vision transformers and convolutional neural networks for image classification: A literature review," *Appl. Sci.*, vol. 13, no. 9, 2023, Art. no. 5521, doi: [10.3390/app13095521](#).
- [27] A. Vaswani et al., "Attention is all you need," in *Proc. Adv. Neural Inf. Process. Syst.*, 2017, pp. 6000–6010.
- [28] E. Arkin, N. Yadikar, X. Xu, A. Aysa, and K. Ubul, "A survey: Object detection methods from CNN to transformer," *Multimedia Tools Appl.*, vol. 82, pp. 21353–21383, 2023, doi: [10.1007/s11042-022-13801-3](#).
- [29] H. Thisanake, C. Deshan, K. Chamith, S. Seneviratne, R. Vidanaarachchi, and D. Herath, "Semantic segmentation using vision transformers: A survey," *Eng. Appl. Artif. Intell.*, vol. 126, 2023, Art. no. 106669, doi: [10.1016/j.engappai.2023.106669](#).
- [30] Z. Liu et al., "KAN: Kolmogorov-Arnold network," in *Proc. Int. Conf. Learn. Representations*, 2025. [Online]. Available: <https://openreview.net/forum?id=Ozo7qJ5vZi>
- [31] C. J. Vaca-Rubio, L. Blanco, R. Pereira, and M. Caus, "Kolmogorov-arnold networks (KANs) for time series analysis," 2024, *arXiv:2405.08790*.
- [32] K. Hornik, M. Stinchcombe, and H. White, "Multilayer feedforward networks are universal approximators," *Eng. Appl. Artif. Intell.*, vol. 2, no. 5, pp. 359–366, 1989, doi: [10.1016/0893-6080\(89\)90020-8](#).
- [33] A. N. Kolmogorov, "On the representation of continuous functions of several variables by superpositions of continuous functions of a smaller number of variables," *Dokl. Akad. Nauk SSSR*, vol. 108, no. 2, pp. 179–182, 1956.
- [34] J. Braun and M. Griebel, "On a constructive proof of Kolmogorov's superposition theorem," *Constructive Approximation*, vol. 30, pp. 653–675, 2009, doi: [10.1007/s00365-009-9054-2](#).
- [35] M. Cheon, "Kolmogorov-Arnold network for satellite image classification in remote sensing," 2024, *arXiv:406.00600*.
- [36] A. Dosovitskiy et al., "An image is worth 16 × 16 words: Transformers for image recognition at scale," in *Proc. Int. Conf. Learn. Representations*, 2021. [Online]. Available: <https://openreview.net/forum?id=YicbFdNTTy>
- [37] Z. Husain and P. Liatsis, "Improved tactile stimulus reconstruction in electrical impedance tomography using the discrete cosine transform and machine learning," *IEEE Sensors J.*, vol. 24, no. 14, pp. 22084–22095, Jul. 2024, doi: [10.1109/JSEN.2023.3338246](#).
- [38] I. Amin, R. Kang, H. AlMarzouqi, Z. Aung, and P. Liatsis, "Convolutional neural network with learnable masks for EIT based tactile sensing," in *Proc. IEEE Int. Conf. Image Process.*, Abu Dhabi, UAE, 2024, pp. 1609–1615, doi: [10.1109/ICIP51287.2024.10647806](#).
- [39] Z. Husain, N. A. Madjid, and P. Liatsis, "Tactile sensing using machine learning-driven electrical impedance tomography," *IEEE Sensors J.*, vol. 21, no. 10, pp. 11628–11642, May 2021, doi: [10.1109/JSEN.2021.3054870](#).
- [40] G. H. Golub, P. C. Hansen, and D. P. O'Leary, "Tikhonov regularization and total least squares," *SIAM J. Matrix Anal. Appl.*, vol. 21, no. 1, pp. 185–194, 1999, doi: [10.1137/S0895479897326432](#).
- [41] D. Maciejewski, Z. Putowski, M. Czok, and L. J. Krzych, "Electrical impedance tomography as a tool for monitoring mechanical ventilation. an introduction to the technique," *Adv. Med. Sci.*, vol. 66, no. 2, pp. 388–395, Aug. 2021, doi: [10.1016/j.advms.2021.07.010](#).
- [42] A. Fedorov et al., "3D slicer as an image computing platform for the quantitative imaging network," *Magn. Reson. Imag.*, vol. 30, no. 9, pp. 1323–1341, Nov. 2012, doi: [10.1016/j.mri.2012.05.001](#).
- [43] A. Adler and W. R. B. Lionheart, "Uses and abuses of EIDORS: An extensible software base for EIT," *Physiol. Meas.*, vol. 27, no. 5, pp. 25–42, May 2006, doi: [10.1088/0967-3334/27/5/S03](#).
- [44] S. Elfving, E. Uchibe, and K. Doya, "Sigmoid-weighted linear units for neural network function approximation in reinforcement learning," *Neural Netw.*, vol. 107, pp. 3–11, Nov. 2018, doi: [10.1016/j.neunet.2017.12.012](#).
- [45] K. Clark et al., "The cancer imaging archive (TCIA): Maintaining and operating a public information repository," *J. Digit. Imag.*, vol. 26, no. 6, pp. 1045–1057, Jul. 2013, doi: [10.1007/s10278-013-9622-7](#).
- [46] G. D. Hugo et al., "A longitudinal four-dimensional computed tomography and cone beam computed tomography dataset for image-guided radiation therapy research in lung cancer," *Med. Phys.*, vol. 44, no. 2, pp. 762–771, Feb. 2017, doi: [10.1002/mp.12059](#).
- [47] C. F. G. D. Santos and J. P. Papa, "Avoiding overfitting: A survey on regularization methods for convolutional neural networks," *ACM Comput. Surveys*, vol. 54, no. 10, pp. 1–25, Jan. 2022, doi: [10.1145/3510413](#).
- [48] A. Adler et al., "GREIT: A unified approach to 2D linear EIT reconstruction of lung images," *Physiol. Meas.*, vol. 30, no. 6, pp. 35–55, Jun. 2009, doi: [10.1088/0967-3334/30/6/S03](#).



- [49] Y. Wu et al., "Shape reconstruction with multiphase conductivity for electrical impedance tomography using improved convolutional neural network method," *IEEE Sensors J.*, vol. 21, no. 7, pp. 9277–9287, Apr. 2021, doi: [10.1109/JSEN.2021.3050845](https://doi.org/10.1109/JSEN.2021.3050845).
- [50] M. Darbas, J. Heleine, R. Mendoza, and A. C. Velasco, "Sensitivity analysis of the complete electrode model for electrical impedance tomography," *Aims Math.*, vol. 6, no. 7, pp. 7333–7366, Sep. 2021, doi: [10.3934/math.2021431](https://doi.org/10.3934/math.2021431).
- [51] A. Adler, "GREIT: Adult thorax example," Eidors, Accessed: Feb. 18, 2025. [Online]. Available: [https://eidors3d.sourceforge.net/tutorial/GREIT/adult\\_ex.shtml](https://eidors3d.sourceforge.net/tutorial/GREIT/adult_ex.shtml)



**IBRAR AMIN** received the bachelor's (Hons.) degree in computer science from COMSATS, Islamabad, Pakistan, in 2017, and the M.S. degree from the Kohat University of Science and Technology, Kohat, Pakistan, in 2021. He is currently working toward the Ph.D. degree from the Khalifa University of Science and Technology, Abu Dhabi, UAE. His research interests include machine learning and deep learning, and their applications in healthcare.



**SHUAIKAI SHI** received the B.S. degree in applied physics from Taiyuan Normal University, Taiyuan, China, in 2016, the M.S. degree in Physics from Tongji University, Shanghai, China, in 2019, and the Ph.D. degree from Northwestern Polytechnical University, Xi'an, China, in 2023. He is currently a Postdoctoral Researcher with Khalifa University, Abu Dhabi, UAE. His research interests include Bayesian machine learning and its applications in hyperspectral image processing, such as unmixing and fusion.



interests include deep learning, artificial intelligence, digital rock physics, and bioinformatics. Dr. Almarzouqi is a member of the IEEE Signal Processing Society.

**HASAN ALMARZOUQI** (Senior Member, IEEE) received the bachelor's (Hons.) and M.Sc. degrees in electrical and computer engineering from Vanderbilt University, Nashville, TN, USA, in 2004 and 2006, respectively, and the Ph.D. degree in electrical and computer engineering from the Georgia Institute of Technology, Atlanta, GA, USA, in 2014. He is currently an Assistant Professor with the Department of Electrical Engineering and Computer Science, Khalifa University of Science and Technology, Abu Dhabi, UAE. His research



**ZEYAR AUNG** (Senior Member, IEEE) received the Ph.D. degree in computer science from the National University of Singapore, Singapore, in 2006. From 2006 to 2010, he was a Research Fellow with the Institute for Infocomm Research, Agency for Science, Technology and Research (A\*STAR), Singapore. In 2010, he joined Masdar Institute, which later became a part of Khalifa University, as an Assistant Professor. He is currently an Associate Professor with the Department of Computer Science, Khalifa University. His past research interests

include bioinformatics and chemoinformatics. His current research interests include data analytics, machine learning, and their applications in various domains, such as cyber security, social media, renewable energy, and power systems.



**WAQAR AHMED** received the bachelor's (Hons.) and M.Sc. degrees in electronic engineering from PAF-Karachi Institute of Economics and Technology, Karachi, Pakistan, in 2012 and 2015, respectively, and the Ph.D. degree in pattern analysis and computer vision from the University of Genoa, Genoa, Italy, in 2021. He also works as an AI scientist with Silo AI, Finland, and he is currently working toward the Postdoctoral research with Khalifa University of Science and Technology, Abu Dhabi, UAE. His research interests include

image processing, computer vision, and pattern recognition.



**PANOS LIATISIS** (Senior Member, IEEE) received the diploma degree in electrical engineering from the University of Thrace, Xanthi, Greece, in 1990, and the Ph.D. degree in electrical engineering and electronics from the University of Manchester, Manchester, U.K., in 2002. He commenced his academic career with The University of Manchester. He joined the City, University of London, London, U.K., where he was a Professor and the Head of the Electrical and Electronic Engineering Department. He is currently a Professor with the

Department of Computer Science, Khalifa University of Science and Technology, Abu Dhabi, United Arab Emirates. His research interests include image processing, computer vision, pattern recognition, and machine learning.